IEEE Access
Multidisciplinary | Rapid Review | Open Access Journal

Received 25 March 2023, accepted 27 April 2023, date of publication 3 May 2023, date of current version 10 May 2023.

Digital Object Identifier 10.1109/ACCESS.2023.3272751

RESEARCH ARTICLE

Reaction Force Analysis for Obstacle-Aided Locomotion of Snake Robot Using Piecewise Helixes

TAKURO TAKANASHI[1], MIZUKI NAKAJIMA[1], TATSUYA TAKEMORI[2], AND MOTOYASU TANAKA[1], (Member, IEEE)

[1]Department of Mechanical and Intelligent Systems Engineering, The University of Electro-Communications, Tokyo 182-8585, Japan
[2]Abstract Engine Company Ltd., Tokyo 150-0011, Japan

Corresponding author: Takuro Takanashi (takuro.takanashi@rc.mce.uec.ac.jp)

This work was supported in part by the Japan Society for the Promotion of Science (JSPS) KAKENHI under Grant JP21H01285.

ABSTRACT Snake robots can use numerous joints to move in various manners. One of them is the obstacle-aided locomotion, a method in which a robot moves by pushing obstacles. In our previous study, we proposed a three-dimensional obstacle-aided locomotion using piecewise helixes, which is composed of an obstacle-contacting part and a grounding part. However, this method is imperfect. This is because when depending on the contact condition with obstacles, the reaction force may make it difficult for the robot to maintain contact with the obstacles or to propel itself. In this study, we analyze the reaction force received from obstacles during the obstacle-aided locomotion to improve the performance of the method. Using these analysis results, we evaluate the contact points of the obstacle-contacting part from two perspectives. The first considers the maintenance of contact with the obstacle, and the second considers the factors that interfere with propulsion. The reaction force was confirmed experimentally using a force sensor. Additionally, the theory of the factors that interfere with the propulsion and maintenance of contact with the obstacle was verified using experiments of the obstacle-aided locomotion in several environments.

INDEX TERMS Search and rescue robots, biologically-inspired robots, field robots.

I. INTRODUCTION

Snake robots can perform various movements using numerous joints. Previous studies have reported movement inspired by biological snakes such as sinus-lifting and sidewinding [1], [2], [3]. Additionally, movements such as step climbing [4], ladder climbing [5] and hoop passing motion which are not performed by biological snakes have been proposed. As described above, snake robots can perform a variety of motions and are applicable in searching disaster sites and inspecting factories.

There are many obstacles, such as rubble and pipes, in an environment where snake robots can work with. Therefore, many studies have been conducted on obstacle-aided locomotion, in which robots use obstacles to move. There are various approaches for utilizing obstacles. One of the methods is to control the direction of the reaction force from the obstacle by controlling the link angle of the robot in contact with the obstacle [8], [9], [10]. Using these methods, the robot's body is adapted to an obstacle to easily obtain a propulsive force. Another method is where the robot actively pushes back against the obstacle using its body to gain a propulsive force [11], [12]. In [13], it has been confirmed that obstacle-aided locomotion can be optimized by changing the gait of the robot based on the density of the obstacles. Additionally, in [14], the robot used obstacles not only for propulsion but also for changing the direction of movement of the robot. In all of these approaches, maintaining contact between the robot and obstacles is very important and crucial. In [15], and [16], a method referred to as "EARLI" was proposed to maintain contact with obstacles for as long as possible. It is also important to identify obstacles that can provide a propulsive force to the robot. In [17], and [18], for the above, "Tegotae-based decentralized control" was proposed.

The associate editor coordinating the review of this manuscript and approving it for publication was Huiyu Zhou.

This method is an extension of the method proposed in [19] that uses curvature derivative control [20] and autonomous decentralized control [21]. Hybrid Obstacle-Aided Locomotion (HOAL) using hybrid position and force control has been proposed in [22]. Other than snake robots, obstacle-aided locomotion of an earthworm soft robot was achieved by combining peristaltic motion with lateral bending [23].

In most of these previous studies, the basic motion of snake robots was undulation on a two-dimensional plane. However, the ground on which the snake robot may move on is often uneven, with rubble and other debris. Three-dimensional motion is required in these environments. Biological snakes adapt to three-dimensional terrains by combining vertical and lateral bending [24], [25]. The propulsion method using vertical bending has been proposed even for snake robots [26], [27]. In [11] and [12], the robot was propelled by adapting its body shape to the uneven ground, such as rocky terrain. Similarly, in [28], the robot's body shape was adapted to uneven ground by adding compliance elements to each module of the robot. Moreover, a method that lifts part of the robot to avoid obstacles was proposed to adapt to uneven environments [29].

These studies above only considered the ground environment. However, a collapsed house or industrial plant may have a three-dimensional obstacle environment, such as pipes protruding from all directions, as shown in Fig. 1. In [30], we proposed an obstacle-aided locomotion using piecewise helixes to improve the snake robot's mobility in the obstacle environment by utilizing the obstacles. The shape of the piecewise helixes consists of an obstacle-contacting part and a grounding part. The obstacle-contacting part is a helix shape and contacts the obstacle, whereas the grounding part is a straight line or a circular arc and is grounded. In the proposed method, the robot can be propelled not only by obstacles on a two-dimensional plane but also by overhead obstacles. To adapt to various obstacle environments, a body-shape change method is also proposed. Additionally, a method for moving and turning in any direction in a flat environment without obstacles is proposed, which can easily switch from the obstacle-aided locomotion.

However, this method has some limitations. One is that the robot may not be able to maintain contact with the obstacle due to the reaction forces. This is because depending on the contact conditions during propulsion, the robot may move away from the obstacle by friction force or rotate owing to the reaction force. Moreover, when using an overhead obstacle, the grounding part may be pressed hard against the ground because of the reaction force from the obstacle, which may interfere with propulsion. In [30], in addition to proposing a method, we analyzed the reaction force from the obstacle. However, we only considered maintaining contact with obstacles on a two-dimensional plane. This is not sufficient for the analysis of the reaction force during obstacle-aided locomotion. This is because, when using a three-dimensional obstacle environment, the effect of the reaction force must also be considered in three dimensions. In this study, we aimed to automate the method proposed in [30] by analyzing the reaction force from the obstacle during the obstacle-aided locomotion in three dimensions. Additionally, based on the results of this analysis, we determined the desirable contact conditions from two perspectives: maintenance of contact with the obstacle and factors that interfere with propulsion. If the robot knows this, it can determine what kind of body shape change is effective in a given situation and can automate adaptation to the obstacle environment. In the analysis, we first considered the dependence of the reaction force on the contact points of the robot. The theory was verified by measuring the reaction force using a force sensor. Furthermore, based on the analysis results of the reaction force, we determined the contact conditions that make it easy to maintain contact with the obstacle and to propel itself. This was confirmed in an obstacle-aided locomotion experiment using several obstacle environments. The analysis in this study depends on the body shape curve of the robot and the condition of the connection between the grounding part and the obstacle-contacting part. Therefore, the analysis can be applied even when the obstacle-contacting part does not have a helical shape, as in the previous study. Moreover, it can be applied when the obstacle-contacting part is connected by any torsion angle in various directions to utilize obstacles in any direction.

Previous studies on obstacle-aided locomotion [8], [9], [10], [11], [12], [13], [14], [15], [16] have analyzed the forces received from obstacles during propulsion. However, the analyses of [8], [9], [10], [11], [12], [13], [14], [15], [16] are based on the angle of each link of the robot makes with the obstacle. In contrast, the analysis in this paper is based on a continuous curve of the robot, and not on each link of the robot, Therefore, it is suitable for analysis in obstacle-aided locomotion using a continuous curve approximation method and shift control as in the method of [30]. In addition, previous methods analyzed reaction forces only on a two-dimensional plane. In contrast, the method proposed in this paper performs the analysis in three dimensions. These analyses are necessary to enable the robot to utilize the three-dimensional obstacle environment autonomously in the future.

The rest of this paper is organized as follows. In Section II, we describe our previously proposed method [30]. Section III presents the results of the analysis of the friction and normal forces from an obstacle during the obstacle-aided locomotion. Based on the results of this analysis, Section IV discusses the maintenance of contact with obstacles and Section V discusses the factors that interfere with propulsion. The reaction force analysis in Section III is verified using the reaction force measurement experiment described in Section VI. In Section VII, we observe obstacle-aided locomotion in several obstacle environments and verify that the above theory is correct. A discussion is provided in Section VIII. Finally, Section IX concludes the paper.

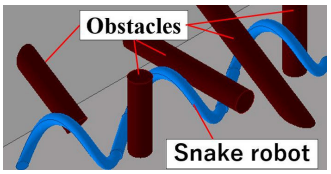

FIGURE 1. Snake robot in cluttered environment [30].

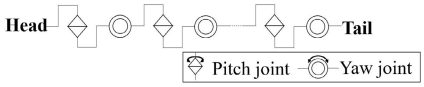

FIGURE 2. Structure of snake robot [30].

II. OBSTACLE-AIDED LOCOMOTION USING PIECEWISE HELIXES [21]

In our previous study, we proposed an obstacle-aided locomotion using piecewise helixes [30]. The shape of the piecewise helixes is shown in Fig. 3. It consists of an obstacle-contacting part and a grounding part. The obstacle-contacting part is an elliptical helix, whereas the grounding part is a straight line or a circular arc. The robot's body shape was fitted to this target curve using the control methods of Yamada and Hirose [31] and Takemori et al. [32]. In this study, we assumed a non-wheeled snake robot as shown in Fig. 2. All the link lengths of this robot are equal, and the pitch and yaw joints are connected alternately.

Each of the obstacle-contacting part and grounding parts is referred to as segment. These two combinations are referred to as segment units. The parameters for each segment are listed in Table 1. $m \in \mathbb{Z}$ denotes the segment unit index. As shown in Fig. 4a, the lengths of the major and minor axes of the obstacle-contacting part (elliptical helix) are denoted by a_j and b_j, respectively. Assuming h_j is the tilt angle of the helix, the pitch of the helix p_j is defined as $2\pi h_j$ (Fig. 4b). The winding angle of the helix is defined as $\phi_j = 2\pi$ in the proposed method. The grounding part is defined by length l_j and curvature κ_j.

In this method, the robot's body shape can be changed and the robot can move by changing the fitting range of the snake robot on the target curve, as shown in Fig. 5. The fitting range can be changed by changing the head position of the robot s_h on the target curve. This is known as shift control [31], [32]. As shown in Fig. 6, the robot can push out an obstacle and propel itself toward the head direction by performing shift control.

We proposed a body shape change method to adapt to various obstacle environments, as shown in Fig. 7. In our method, the shortening (Fig. 7a), extending (Fig. 7b), and bending (Fig. 7c) of the grounding part were proposed. Moreover, the reversal (Fig. 7d) and height adjustment (Fig. 7e) of the obstacle-contacting part were proposed. Using these body shape change methods, the robot can contact obstacles in positions that are not available by the basic shape and can utilize them for propulsion.

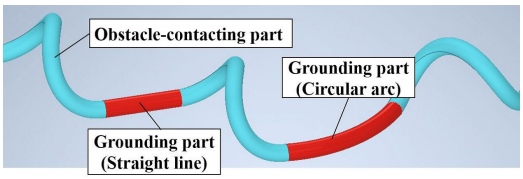

FIGURE 3. Segment configuration of piecewise helixes [30].

TABLE 1. Parameters of segments for the target shape.

seg no. j	part	shape	parameter
$2m+1$	Grounding part	Straight line Circular arc	(l_j, κ_j)
$2m+2$	Obstacle-contacting part	Elliptical Helix	(a_j, b_j, h_j, ϕ_j)

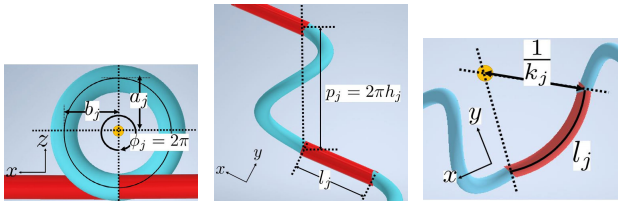

(a) Elliptical helix parameters (b) Definition of elliptical helix pitch (c) Curvature and length of the grounding part

FIGURE 4. Parameters of the target shape [30].

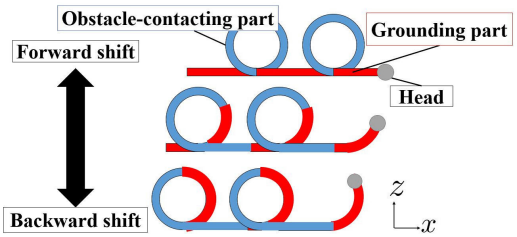

FIGURE 5. Moving by shift control [30].

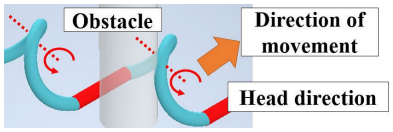

FIGURE 6. Obstacle-aided locomotion [30].

III. ANALYSIS OF REACTION FORCE DURING OBSTACLE-AIDED LOCOMOTION

A. PURPOSE OF ANALYSIS OF REACTION FORCE

When a snake robot performs obstacle-aided locomotion, it is important to propel it easily and maintain contact with the obstacle. In this method, depending on the condition of contact between the robot and obstacle, reaction forces may interfere with the propulsion and maintenance of contact with the obstacles. For contact maintenance with an obstacle geometrically, the theory of form closure [33] is reffered to ensure the robot to be constrained such that it does not move away from the obstacles. In this theory, it is known that at

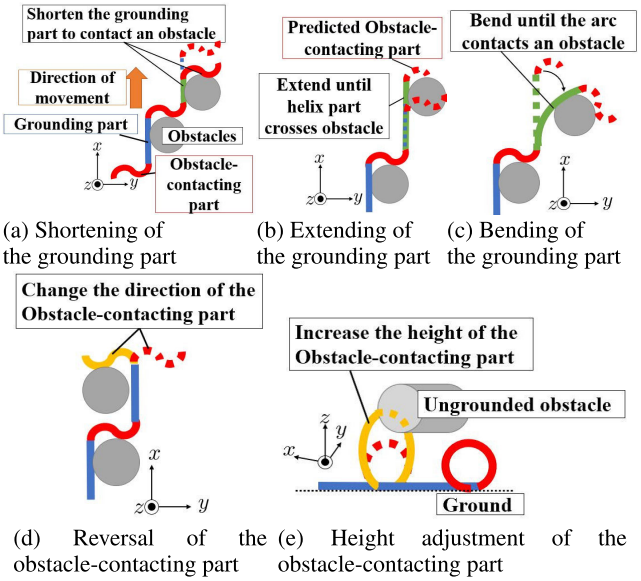

(a) Shortening of the grounding part (b) Extending of the grounding part (c) Bending of the grounding part

(d) Reversal of the obstacle-contacting part (e) Height adjustment of the obstacle-contacting part

FIGURE 7. Body shape changes [30].

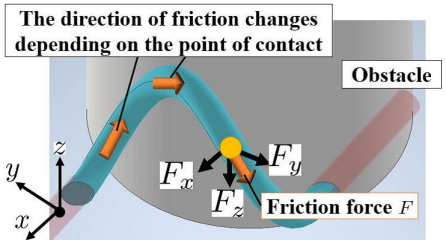

FIGURE 8. Direction of friction force by contact point.

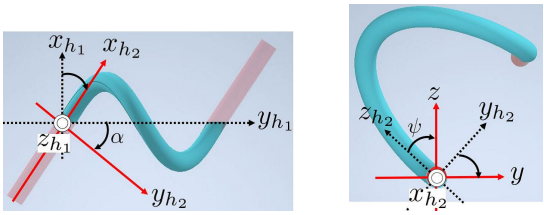

(a) (b)

FIGURE 9. Coordinate conversions. (a) Conversion from coordinate system based on the helix to the coordinate system based on the longitudinal direction of the grounding part. (b) Conversion to the coordinate system that considers the torsional angle ψ at the connection with the grounding part.

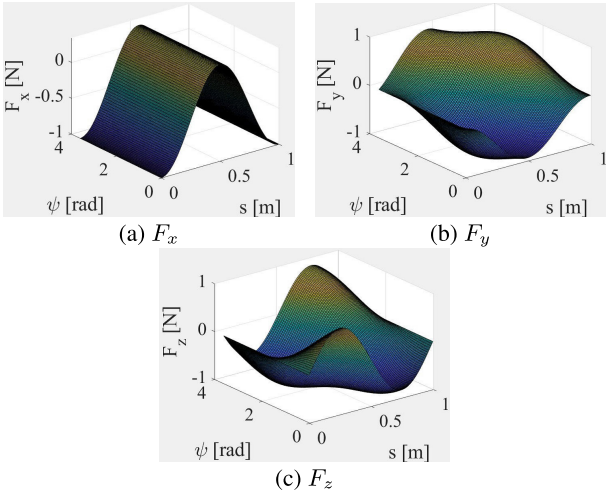

(a) F_x (b) F_y

(c) F_z

FIGURE 10. Variation of friction force with curve length s and torsion angle ψ.

least (degree of freedom of motion + 1) constraint points are required for form closure to be realized. Therefore, at least three constraint points are required to constrain the movement and rotation of the robot, except in the direction of propelling.

In this study, we did not consider the geometrical constraints of movement by the form closure, but rather the constraints of movements by dynamical conditions. This is because the form closure was already known. Moreover, a minimum number of constraint points is required for its realization. This means that there may be situations in which geometrical constraints are impossible depending on the placement of obstacles. Therefore, we considered the friction and normal forces as the reaction forces from the obstacles and how these forces change depending on the point of contact at the obstacle-contacting part.

B. FRICTION FORCE

The direction of the friction force from the obstacle is determined by the direction of movement of the robot body axis on the obstacle surface, as shown in Fig. 8. In this section, we assume that the obstacle-contacting part is connected to the grounding part by an arbitrary torsion angle ψ, as shown in Fig. 9b. We discuss the change in the direction of the friction force depending on the curve length s on the obstacle-contacting part. The following discussion is based on the coordinate system (x, y, z), where x is the longitudinal direction of the grounding part, y is perpendicular to it, and z is perpendicular to the ground. The components of the friction force in each direction are denoted as (F_x, F_y, F_z).

First, we assume that the obstacle-contacting part is a helix, expressed by the following equation:

$$\boldsymbol{C}(\theta_h) = \begin{cases} x_{h1} = r_h \sin\theta_h, \\ y_{h1} = h\theta_h, \\ z_{h1} = r_h \cos\theta_h. \end{cases} \tag{1}$$

where r_h denotes the helix radius, h denotes the tilt angle of the helix, and θ_h denotes the winding angle. The above equation in the curve length parameter form is as follows:

$$\boldsymbol{C}(s) = \begin{cases} x_{h1} = r_h \sin\left(\dfrac{1}{\sqrt{r_h^2 + h^2}} \cdot s\right), \\ y_{h1} = h \cdot \dfrac{1}{\sqrt{r_h^2 + h^2}} \cdot s, \\ z_{h1} = r_h \cos\left(\dfrac{1}{\sqrt{r_h^2 + h^2}} \cdot s\right). \end{cases} \tag{2}$$

To obtain the direction of movement of the robot on the obstacle surface, it is necessary to obtain the vector of the robot's body axis. This vector is obtained by differentiating (2) with s as follows:

$$\begin{bmatrix} \Delta x_{h1} \\ \Delta y_{h1} \\ \Delta z_{h1} \end{bmatrix} = \boldsymbol{C'}(s) = \begin{bmatrix} \frac{r_h}{\sqrt{r_h^2+h^2}} \cos\left(\frac{1}{\sqrt{r_h^2+h^2}} \cdot s\right) \\ h \cdot \frac{1}{\sqrt{r_h^2+h^2}} \\ \frac{-r_h}{\sqrt{r_h^2+h^2}} \sin\left(\frac{1}{\sqrt{r_h^2+h^2}} \cdot s\right) \end{bmatrix}. \quad (3)$$

However, the vector of the robot's body axis obtained by (3) is expressed in the coordinate system (x_{h1}, y_{h1}, z_{h1}) based on the helix. Therefore, it is necessary to convert this to the (x, y, z) coordinate system.

First, it is necessary to consider the torsion angle at the connection between the grounding part and the obstacle-contacting part. Therefore, the coordinate system converts from (x_{h1}, y_{h1}, z_{h1}) to (x_{h2}, y_{h2}, z_{h2}) as shown in Fig. 9a. The longitudinal direction of the grounding part is x_{h_2} and perpendicular to it is y_{h2}. To convert to this coordinate system, it is rotated around the z_{h1} axis by α as follows:

$$\begin{bmatrix} x_{h2} \\ y_{h2} \\ z_{h2} \end{bmatrix} = \begin{bmatrix} \cos\alpha & -\sin\alpha & 0 \\ \sin\alpha & \cos\alpha & 0 \\ 0 & 0 & 1 \end{bmatrix} \begin{bmatrix} x_{h1} \\ y_{h1} \\ z_{h1} \end{bmatrix}, \quad (4)$$

where α is obtained from the shape parameters of the helix as $\alpha = \tan^{-1} h/r_h$.

Next, we consider the case in which the grounding part and obstacle-contacting part are connected by a torsion angle ψ, as shown in Fig. 9b. It is necessary to convert the coordinate system (x_{h2}, y_{h2}, z_{h2}) to (x, y, z) by rotating around the x_{h2} axis by ψ as follows:

$$\begin{bmatrix} x \\ y \\ z \end{bmatrix} = \begin{bmatrix} 1 & 0 & 0 \\ 0 & \cos\psi & -\sin\psi \\ 0 & \sin\psi & \cos\psi \end{bmatrix} \begin{bmatrix} x_{h2} \\ y_{h2} \\ z_{h2} \end{bmatrix}. \quad (5)$$

Based on the above, the vector of the robot's body axis after conversion from the coordinate system (x_{h1}, y_{h1}, z_{h1}) to (x, y, z) is as follows:

$$\begin{bmatrix} \Delta x \\ \Delta y \\ \Delta z \end{bmatrix} = \boldsymbol{R}_\psi \boldsymbol{R}_\alpha \begin{bmatrix} \Delta x_{h1} \\ \Delta y_{h1} \\ \Delta z_{h1} \end{bmatrix}, \quad (6)$$

where $\boldsymbol{R}_\alpha$ and $\boldsymbol{R}_\psi$ denote the rotation matrices of (4) and (5), respectively.

We assume that a constant friction force F acts in the direction of the body axis of the robot. Using the unit vector of the robot's body axis obtained by (6), the friction force (F_x, F_y, F_z) in each direction is obtained as follows:

$$\begin{bmatrix} F_x \\ F_y \\ F_z \end{bmatrix} = F \cdot \frac{1}{\sqrt{\Delta x^2 + \Delta y^2 + \Delta z^2}} \begin{bmatrix} \Delta x \\ \Delta y \\ \Delta z \end{bmatrix}. \quad (7)$$

From (7), it is possible to obtain the friction force in each direction with torsion angle ψ and curve length s of the obstacle-contacting part. We assume that the friction force $F = 1.0$[N] is always constant. The variation in the friction force in each direction with s and ψ can be obtained as shown in Fig. 10. It is considered that the value of each directional component of the friction force affects the ease of contact maintenance with the obstacle and the propulsion of the robot. The curve length s in these plots is normalized to zero at the head and one at the tail of the obstacle-contacting part. The same normalization is applied to s in the rest of this study.

C. NORMAL FORCE

The direction of the normal force N received from the obstacle is also determined by the body shape of the obstacle-contacting part. The absolute value of N was assumed to be constant, and we focused only on the direction of the force. The plane in contact with the obstacle was defined as the obstacle-contacting plane, as shown in Fig. 11a (red box in this figure), and the normal force was acting perpendicular to this plane.

First, we define the obstacle-contacting plane. Let $\boldsymbol{T}$ be the robot's body axis vector and $\boldsymbol{n}$ be the normal vector of the plane formed by $\boldsymbol{T}$ and the x-axis unit vector, respectively. The obstacle-contacting plane is the plane formed by $\boldsymbol{T}$ and $\boldsymbol{n}$ as shown in Fig. 11b. $\boldsymbol{n}$ is the cross product of $\boldsymbol{T} = [\Delta x, \Delta y, \Delta z]$ obtained in the previous section and the unit vector $[1, 0, 0]$ in the x-axis direction as follows:

$$\boldsymbol{n} = \begin{bmatrix} \Delta x \\ \Delta y \\ \Delta z \end{bmatrix} \times \begin{bmatrix} 1 \\ 0 \\ 0 \end{bmatrix} = \begin{bmatrix} 0 \\ \Delta z \\ -\Delta y \end{bmatrix}. \quad (8)$$

The normal force N from the obstacle acts in the direction of the vector $\boldsymbol{B}$ perpendicular to the obstacle-contacting plane defined above. $\boldsymbol{B}$ is the cross product of vectors $\boldsymbol{T}$ and $\boldsymbol{n}$ as follows:

$$\boldsymbol{B} = \begin{bmatrix} \Delta x \\ \Delta y \\ \Delta z \end{bmatrix} \times \begin{bmatrix} 0 \\ \Delta z \\ -\Delta y \end{bmatrix} = \begin{bmatrix} -\Delta y^2 - \Delta z^2 \\ \Delta x \cdot \Delta y \\ \Delta x \cdot \Delta z \end{bmatrix}. \quad (9)$$

Fig. 12 shows the body shape of the obstacle-contacting part (blue line), vector $\boldsymbol{n}$ (orange line), and vector $\boldsymbol{B}$ (yellow line). The obstacle-contacting plane is the plane formed by $\boldsymbol{n}$ and the robot's body shape curve. The plot shows that the normal force acts vertically at both ends of the obstacle-contacting part and is almost parallel to the ground at its midpoint.

From the above, the reaction force received from the obstacle can be obtained in three dimensions. This enables us to consider the effect of the reaction forces based on the point of contact between the obstacle and the obstacle-contacting part in three dimensions. In our previous study [30], we derived the conditions under which the robot maintains contact with the obstacle by analyzing the reaction force. However, the analysis was imperfect because the direction of the normal force from the obstacle was assumed to be normal to the curved surface of the obstacle in the analysis. In this case, in order for the robot to automatically determine whether

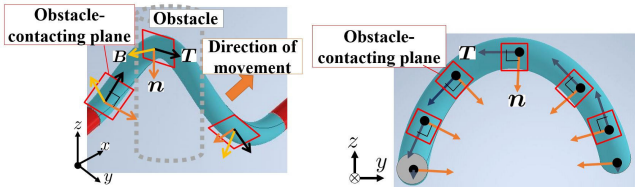

FIGURE 11. Definition of the obstacle-contacting plane and each vector. (a) The obstacle-contacting plane and vectors T, B, n. (b) These vectors in the $y-z$ plane.

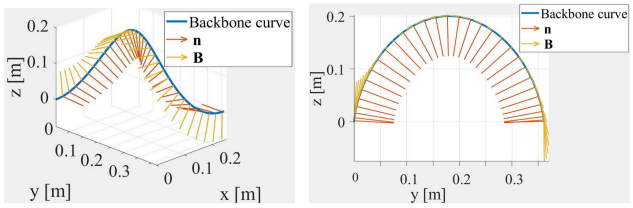

FIGURE 12. Result of drawing each vector. (a) Robot body shape and vectors B, n. (b) Vectors in the $y-z$ plane.

or not it can maintain contact, the curvature of the obstacle surface must be measured by a sensor, such as a vision sensor. In addition, we only considered the robot's movement on a two-dimensional plane due to a reaction force. Furthermore, we did not consider that reaction forces can sometimes cause the robot to rotate around the point of contact or interfere with propulsion. Therefore, in Sections IV and V, we will consider the effects of reaction forces on contact maintenance, including rotation, and factors interfering with propulsion in three dimensions. Both the normal force and the friction force are obtained from the body shape curve; therefore, the analysis in this paper is independent of the information on the obstacle.

IV. CONDITIONS FOR MAINTAINING CONTACT WITH OBSTACLES

Based on the analysis of the reaction force from the obstacle in Section III, we discuss the conditions for maintaining contact with obstacles based on the point of contact in the obstacle-contacting part. There are two possible situations in which the robot cannot maintain contact with the obstacle, as shown in Fig. 13. Fig. 13a is a situation in which the robot cannot move smoothly on the obstacle surface because of friction. In this situation, the robot may move in the $-y$ direction in this figure, which is referred to as moving sideways in the following. Fig. 13b is a situation in which the robot rotates owing to the moment caused by the reaction force from the obstacle.

A. MOVING SIDEWAYS

Moving sideways (Fig. 13a) is caused by F_y, which is the y direction of the friction force with the obstacle. Fig. 10b shows that the absolute value of F_y is smaller when the curve length s is large or small (both ends of the obstacle-contacting part), regardless of the torsional angle ψ. However, the absolute value of F_y is larger at the midpoint of the obstacle-contacting part. Additionally, F_y is negative when $\psi = 0$ and positive when $\psi = \pi$. In both cases, sideways movement is more likely to occur when the absolute value of F_y is particularly large. Therefore, the midpoint of the obstacle-contacting part was the point at which this problem was most likely to occur.

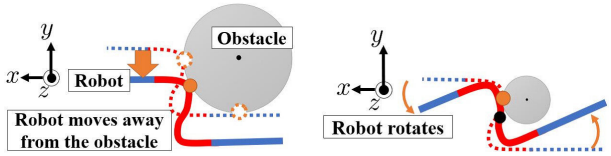

FIGURE 13. When the robot cannot maintain contact with obstacles.

Next, we consider the case in which multiple obstacles are utilized in several patterns, as shown in Fig. 14. Fig. 14a shows the case in which multiple obstacles are on the same side. In this case, F_{y_i} (where i is the segment unit number), which is the friction force component in the y-direction, acts in the same direction. Therefore, the $(F_{y_1} + F_{y_2})$ forces easily move the robot in the $-y$ direction in the figure. However, F_{y_i} act in the opposite direction at the reversed obstacle-contacting part, as shown in Fig. 14b. Therefore, the force that moves the robot sideways is the difference between F_{y_i} received by the obstacle-contacting part in the basic and reversed shapes. Finally, Fig. 14c shows the case in which the grounding part is bent. In this case, the ease of moving sideways and its direction can be determined by synthesizing the friction force of the y component at each obstacle-contacting part. This is obtained using the angle between F_{y_i} and the x axis $\theta_r = \kappa_j \cdot l_j$, where κ_j is the curvature of the grounding part and l_j is its length.

B. ROTATION

1) FACTORS THAT MAKE THE ROBOT ROTATE

Rotation (Fig. 13b) is caused by the moment around the center of gravity of the robot due to the reaction force from the obstacle. First, as illustrated in Fig. 15, we focus on only one obstacle-contacting part, excluding the grounding part. We assumed that the center of gravity was the midpoint of the obstacle-contacting part.

Reaction force $\boldsymbol{R}$ in Fig. 15 is the combined normal force $\boldsymbol{N}_{xy}$ and friction force $\boldsymbol{F}_{xy}$ which are projected on the $x-y$ plane. The normal force $\boldsymbol{N}_{xy}$ is the unit vector of the (x, y) components of $\boldsymbol{B}$ defined in Section III-C. The value of the friction force $\boldsymbol{F}$ is the absolute value of $\boldsymbol{B}$ ($|\boldsymbol{B}| = 1$) multiplied by the friction coefficient μ and unit vector of the robot's body axis vector $\boldsymbol{T}$ ($\boldsymbol{F} = \mu \cdot \boldsymbol{T}$). The above x, y components are used as $\boldsymbol{F}_{xy}$. Using these forces, the reaction force received from the obstacle was defined as $\boldsymbol{R} = \boldsymbol{N}_{xy} + \boldsymbol{F}_{xy}$.

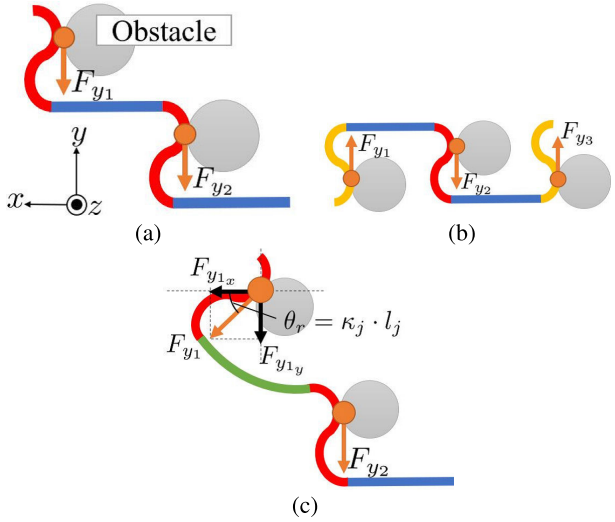

FIGURE 14. Synthesis of forces related to moving sideways when (a) all obstacle-contacting parts are in the same direction, (b) there is a reversed one and (c) the grounding part is bent.

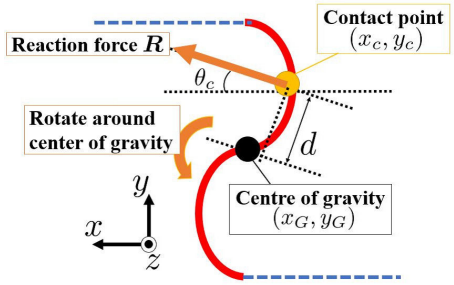

FIGURE 15. Moment around the center of gravity of the obstacle-contacting part due to the reaction force.

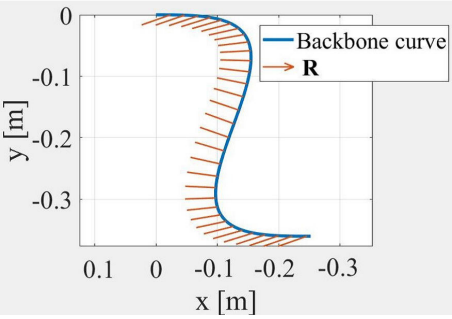

FIGURE 16. Drawing result of the backbone curve and direction of the reaction force at the obstacle-contacting part when $\mu = 0$.

The vertical distance d from the center of gravity to the reaction force $\boldsymbol{R}$ shown in Fig. 15 is obtained as follows:

$$d = \sqrt{(x_c - x_G)^2 + (y_c - y_G)^2} \cdot \sin\left(\frac{\pi}{2} + \theta_c - \tan^{-1}\frac{|x_c - x_g|}{|y_c - y_G|}\right), \quad (10)$$

where θ_c is the angle between the reaction force $\boldsymbol{R}$ and the x axis and is obtained as $\theta_c = \tan^{-1} R_x/R_y$. It should be noted that R_x and R_y are the x and y components of $\boldsymbol{R}$. The coordinates of the center of gravity are (x_G, y_G) and the coordinates of the contact point are (x_c, y_c). Using the above, the moment around the center of gravity M_G of the robot can be calculated using the absolute values of the x, y components of the reaction force $|\boldsymbol{R}_{xy}| = \sqrt{R_x^2 + R_y^2}$ as $M_G = d \cdot |\boldsymbol{R}_{xy}|$.

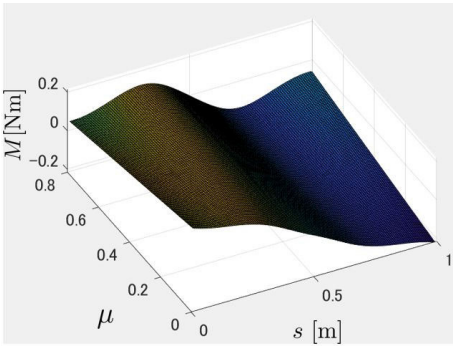

FIGURE 17. Variation of moment with friction coefficient μ and curve length s.

Fig. 16 shows the body shape curve and direction of the reaction force at the obstacle-contacting part. Fig. 16 shows the case with a friction coefficient $\mu = 0$. As the friction coefficient increases, $\boldsymbol{R}$ tilts more toward the negative direction of the y axis, and the value of the moment also changes. Fig. 17 shows the change of the moment with the curve length s and friction coefficient μ. It should be noted that the counterclockwise direction shown in Fig. 16 is defined as the positive direction. Fig. 17 shows that when the friction coefficient is small, the moment is particularly large when the value of s is large and small. Therefore, the robot tend to rotate when it make contact at both ends of the obstacle-contacting part. However, the robot is less likely to rotate near the midpoint of the obstacle-contacting part. Comparing the case with a large friction coefficient and that with a small friction coefficient, the trend is similar for both cases. However, the absolute value of the moment at both ends is smaller when the coefficient of friction is larger than when it is smaller.

These results suggest that the ease of rotation depends not only on the point of contact at the obstacle-contacting part but also on the value of the friction coefficient on the surface of the obstacle. This is particularly clear at both ends of the obstacle-contacting part.

Next, we consider the case of contact with obstacles in multiple obstacle-contacting parts. In this case, the ease of rotation of the robot is determined by the sum of the moments around the center of gravity of the robot owing to the reaction forces at each contact point. First, we determine the position of the robot's center of gravity as follows: The target continuous curve in the range fitted to the robot was represented by the (x, y, z) coordinate system. The weight of the robot in the micro-interval ds of the curve is obtained as $m_i = \rho \cdot ds$, where ρ is the line density of the robot, which is assumed to be constant throughout the robot. Using the above equation and

the coordinates (x_i, y_i) of each point of the robot, the position of the center of gravity $G(x_G, y_G)$ on the x, y plane is obtained as follows:

$$\begin{cases} x_G = \dfrac{ds(x_1 + x_2 + x_3 + \cdots)}{ds(l_{rob}/ds)}, \\ y_G = \dfrac{ds(y_1 + y_2 + y_3 + \cdots)}{ds(l_{rob}/ds)}. \end{cases} \tag{11}$$

where l_{rob} is the length of the robot and l_{rob}/ds is the number of divisions. The origin of the $x - y$ coordinate system is set at the head of the robot.

As shown in Fig. 18, the contact point C_i can also be represented in the $x - y$ coordinates. In the case of Fig. 18a, the moment of the robot is obtained as follows:

$$M_{all} = d_1 \cdot |\boldsymbol{R}_1| - d_2 \cdot |\boldsymbol{R}_2 \boldsymbol{R}_2| \tag{12}$$

d_i in above equation is obtained by the following equation using the coordinates of each contact point:

$$d_i = \sqrt{(x_{c_i} - x_G)^2 + (y_{c_i} - y_G)^2} \cdot \sin\left(\frac{\pi}{2} + \theta_{ci} - \tan^{-1}\frac{|x_{c_i} - x_G|}{|y_{c_i} - y_G|}\right), \tag{13}$$

where θ_{c_i} is the angle between the direction of the reaction force and x axis. If the grounding part is bent, as shown in Fig. 18b, the direction of the reaction force $\boldsymbol{R}$ changes by θ_r in the figure. Therefore, $\theta'_{c_1} = \theta_{c_1} + \theta_r$ in Fig. 18b can be substituted into θ_{c_i} in the above equation to obtain d_i and the moment in the same way.

If the points of contact with multiple obstacles can be adjusted such that the absolute value of the moment M_all calculated above decreases, rotation may be prevented. To assist the operator in making this adjustment decision during robot operation, we created a system. This system draws the target curve of the robot in the $x - y$ plane, the position of the center of gravity, and the direction of the reaction force of the obstacle-contacting part. The results are presented in Fig. 19. This system also responds to shift control and body shape changes of the robot. It can always draw the robot's body shape, center of gravity, and reaction force at any given point in time. We believe that it is possible to realize a contact state that prevents rotation by instructing the body to change its shape based on the drawing result of this system.

For example, if the point of contact with an obstacle is known, the positional relationship between the center of gravity and direction of the reaction force at the point of contact can be determined. Therefore, it is possible to predict how likely the robot is to rotate at that instant. As shown in Fig. 20a, we considered the case in which the robot is in contact with obstacle 4 at its tail. In this case, a large clockwise moment is expected to be generated by observing the direction of the drawn reaction force, and the robot is expected to rotate. We assume that there are obstacle candidates 1-3 available and we know the direction of the reaction force generated by contact with each obstacle using this system. In this figure, we observe that contact with obstacle 1 generates a moment of the same value in the direction opposite

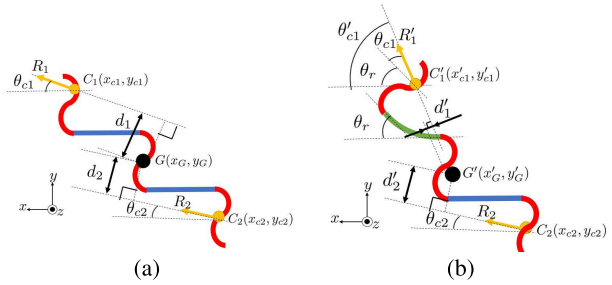

FIGURE 18. Moments throughout the robot when receiving reaction forces from multiple obstacles. (a) In the case of the basic shape. (b) In the case where the grounding part is bent.

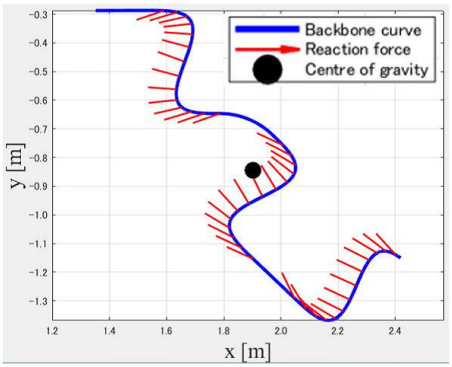

FIGURE 19. Example of drawing of the center of gravity and reaction force at the obstacle-contacting part.

to the moment due to contact with obstacle 4, which prevents rotation. Therefore, the operator can choose to shorten the grounding part to make the head obstacle-contacting part come into contact with obstacle 1. Next, we considered the case where the robot was in contact with several obstacles, as shown in Fig. 20b. The system can identify obstacles that generate large moments and can decide to shorten the rear grounding part to avoid contact with obstacle 2.

2) FACTORS THAT PREVENT THE ROTATION OF THE ROBOT

We focused on the obstacle-contacting part in the above discussion of the rotation of the robot. However, when considering the grounding part, some factors can prevent rotation, such as friction between the grounding part and ground and the moment of inertia of the robot.

First, we considered the moment of inertia around the center of gravity of the robot when it was assumed to be a rigid body. As shown in Fig. 21a, we assumed the case in which the robot rotates around its center of gravity with an angular acceleration of $\dot{\omega}$. The effect of friction is not considered. Let $r(s)$ be the shortest distance from the center of gravity to a point of any curve length s. The total moment of inertia I is obtained by integrating the moment of inertia of a micro-interval ds from the head position to the center of gravity of

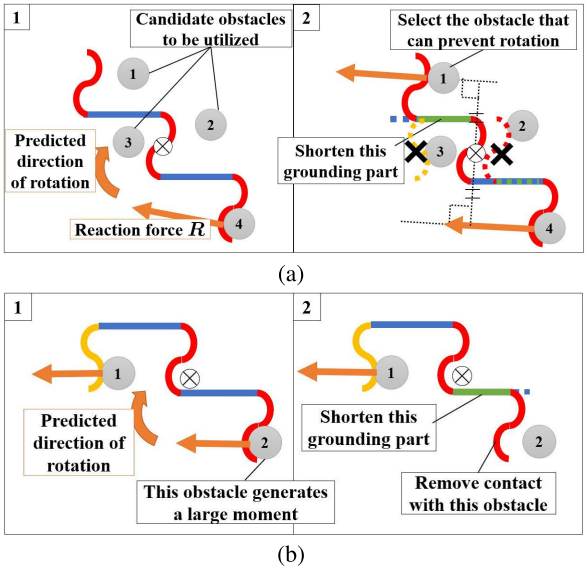

FIGURE 20. Examples of using a program to draw the position of the center of gravity and reaction force. (a) Select obstacles that can prevent rotation. (b) Release contact with obstacles that cause rotation.

the robot, as follows:

$$I = \int_{s_G}^{s_h} r(s)^2 \cdot \rho \cdot \pi \cdot R_{link}^2 \, ds, \tag{14}$$

where s_G is the curve length at which the center of gravity is located and s_h is the curve length at the head position of the robot. The mass of the robot in micro-interval ds is expressed as $\rho \cdot \pi \cdot R_{link}^2 \cdot ds$, where R_{link} is the link radius of the robot.

The torque τ used to rotate the robot was calculated from the equation of motion of rotation using the angular acceleration $\dot{\omega}$ as follows:

$$I \cdot \dot{\omega} = \tau, \tag{15}$$

where we assume that a constant torque τ is always obtained from the obstacle, regardless of the robot's body length. From (14), it can be concluded that I increases as the robot's body length increases. Consequently, from (15), the angular acceleration $\dot{\omega}$ is smaller. In other words, it is thought that rotation is less likely to appear when the robot's body length is longer, even in the same case of the obstacle-aided locomotion.

Next, we consider the effect of the friction force between the grounding parts and the ground. We assumed that the robot rotates in a counterclockwise direction around its center of gravity, and that the friction force F_{gi} acts in a direction perpendicular to the vertical distance d_i from the center of gravity at the midpoints of each grounding part. Fig. 21b shows that the moment $M_i = d_i \cdot F_{gi}$ around the center of gravity of the robot acts at the midpoint of each grounding part in the opposite direction to the direction of rotation. The sum of these moments prevents rotation. Moreover, in the case shown in Fig. 21b, the moment generated by F_{g2} at the second grounding part from the center of gravity has a significant effect on rotation prevention.

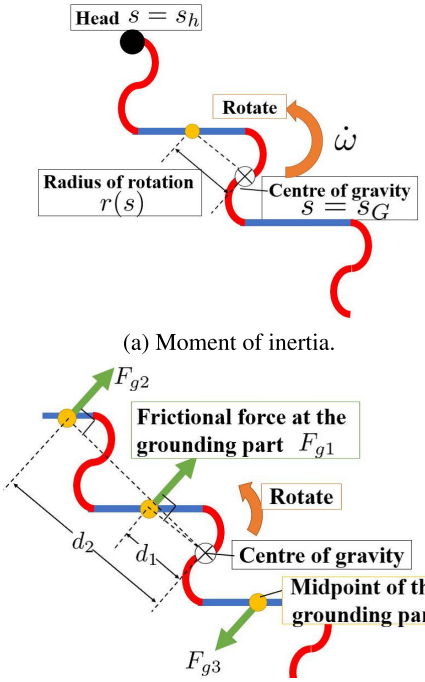

FIGURE 21. Factors that can prevent rotation.

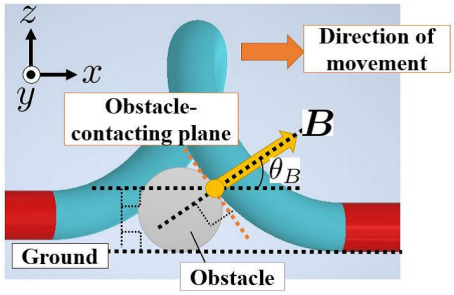

FIGURE 22. Angle θ_B between the ground plane and obstacle-contacting plane.

From the above, the longer the robot's body length, the more difficult it is to rotate, owing to the effect of the moment of inertia. Additionally, if the grounding part is located far from the center of gravity, the rotation can be further prevented by the moment generated by the frictional force at the grounding part. Therefore, if rotation is not desired, it is effective to increase the robot's body length and set the grounding part to be located far away from the center of gravity of the robot.

V. FACTORS INTERFERING WITH PROPULSION

This section describes another factor that affects obstacle-aided locomotion: the forces that interfere with propulsion. Depending on the direction of the normal force or friction force received from the obstacle, a force may be

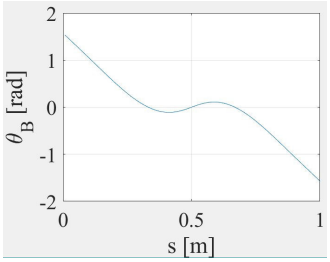

FIGURE 23. Variation of θ_B with curve length s.

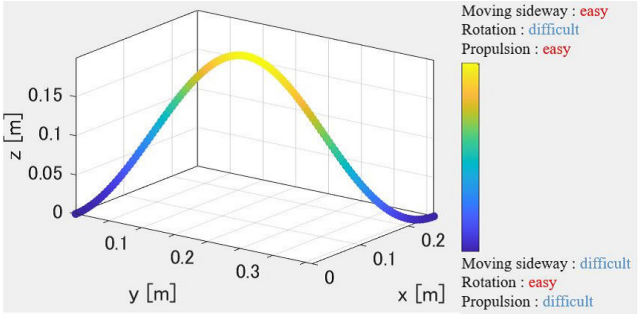

FIGURE 24. Body shape curve and evaluation of the obstacle-contacting part.

generated that interferes with the propulsion of the robot during obstacle-aided locomotion.

First, we discuss the effect of the direction of the normal force on propulsion, as obtained in Section III-C. The direction of the normal force varied depending on the point of contact, as shown in Fig. 12. When the direction of the normal force is horizontal, most of it can be used for propulsion purposes. However, problems arise when the normal force is vertically upwards or downward. In the vertical upward case, the friction force on the surface of the obstacle increased as the load of the robot was added to the pushing force. In the vertical downward case, the normal force pushed the robot against the ground, increasing the friction at the grounding part. These factors interfere with the movement of the body axis of the robot in the direction of propulsion. Then, we focused on the angle θ_B, as shown in Fig. 22, for a discussion of the contact points where the normal force is likely to interfere with propulsion. θ_B is the angle between the normal force and grounding plane when viewed in the $x-z$ plane. It is obtained from the x and z components of vector $\boldsymbol{B}$ obtained by (9) as follows:

$$\theta_B = \tan^{-1} \frac{\Delta x \cdot \Delta z}{-\Delta y^2 - \Delta z^2}. \tag{16}$$

Fig. 23 shows θ_B with the curve length s. This plot shows that the absolute value of θ_B is particularly small when s is approximately 0.5 m. Therefore, it is considered that the situation that prevents the propulsion of the robot mentioned above is unlikely to occur at the midpoint of the obstacle-contacting part. Conversely, when the value of θ_B is negative and large (when s is approximately 1 m), the robot is pressed against the ground by the normal force. This increases the frictional force on the grounding part, making it difficult for the robot to propel itself. In the other hand, when θ_B is positive and large (when s is near 0 m), the robot pushes against the obstacle from above. In this case, the frictional force on the surface of the obstacle increases. This is because the robot's weight is added to the pushing force owing to the movement of the robot, making it more difficult for the robot to propel itself.

The friction force components F_x and F_z obtained by Section III-B also interfere with the propulsion of the robot. First, we discuss F_x. When F_x is negative, it acts in the direction opposite to the direction of propulsion. Therefore, F_x is a force that prevents the robot from moving in the direction of travel on the obstacle surface. Fig. 10a shows that F_x does not change with the value of the torsion angle ψ, but only with the curve length s. Moreover, the absolute value of F_x near both ends of the obstacle-contacting part was the largest at negative values. This indicates that the contact point interferes with the robot from propulsion the most.

Next, we discuss F_z. Fig. 10c shows that the absolute value of F_z is smaller when s is large, small, and near the midpoint. As in the case of F_y, the direction of the force was reversed when ψ was zero and π. When $\psi = 0$, the force is particularly strong in the upward direction near $s = 0.25$ m, and the robot behaves as if it is climbing the surface of an obstacle. At approximately $s = 0.75$ m, this force acts strongly in the downward direction, and is considered to push the robot to the ground. When $\psi = \pi$, this force exhibits the opposite behavior.

The above results indicate that forces that interfere with the propulsion of the robot tend to be generated near both ends of the obstacle-contacting part. Therefore, from this perspective, it is preferable to make contact at the midpoint of the obstacle-contacting part.

At the end of this section, we summarize the theory of the conditions for maintaining contact with obstacles in Section IV and the factors that interfere with the propulsion of the robot discussed above. These are determined by the shape of the obstacle-contacting part. As shown in Fig. 24, contact with the obstacle near the midpoint of the obstacle-contacting part tends to move sideways but prevents rotation. Forces that interfere with the propulsion of the robot are also difficult to generate. At both ends of the obstacle-contacting part, sideways movement was prevented, but rotation was likely to occur. Forces that interfere with the propulsion of the robot are also likely to be generated.

VI. EXPERIMENT OF REACTION FORCE MEASUREMENT

A. EXPERIMENTAL METHOD

The theory of the reaction force at the obstacle-contacting part during the obstacle-aided locomotion, which is discussed in Section III, was experimentally confirmed. In the experiment, a six-axis force sensor and snake robot, as shown in Fig. 25 were used. The robot was the same as that developed

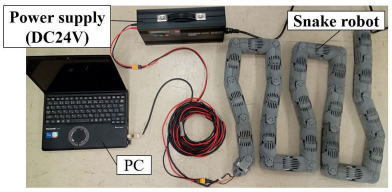

FIGURE 25. Snake robot. [30].

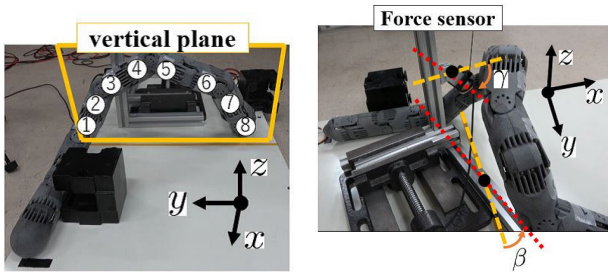

(a) Front view. (b) Side view.

FIGURE 26. Experimental environment of the reaction force measurement.

by [30]. The robot has no wheels, and the pitch and yaw joints were connected alternately. In this robot, the length of each link is 70 mm, the link radius was 28 mm, and the weight of each link is 146 g. In the experiment, the normal and friction forces during the movement were measured on several links of the obstacle-contacting part of the robot. The friction force measurements may be incorrect if the contact state with the obstacle changes gradually during propulsion. Therefore, we performed shift control for a very short period and measured the static friction force at the beginning of the movement instead of the dynamic friction force.

Fig. 26 shows the experimental environment. Eight spots of the obstacle-contacting part were used as measurement points, as shown in Fig. 26a. The angle between the base of the aluminum frame and the sensor was adjusted so that the sensor surface and the direction of the robot's body axis were parallel at each measurement point. From this state, shift control was performed at a very slow shift speed of $\dot{s}_h = 0.2$ mm/s. Measurements were performed three times at each measurement point. The horizontal and vertical forces measured by the force sensor are defined as the friction and normal forces, respectively. After the measurements, the sensor results were converted to the same coordinate system (x, y, z) as in the theory described in the previous section. For the conversion, we used the angle γ between the sensor and the ground surface, and the angle β between the base of the aluminum frame and the y-axis, as shown in Fig. 26b. In the measurement, the static friction force was measured at the moment when the robot started to move both at the head and tail of the robot. The ground surface of the robot is a plate with a small coefficient of friction. The sensor surface was covered with tape to prevent the frictional force measured by the sensor from becoming too small. The static friction

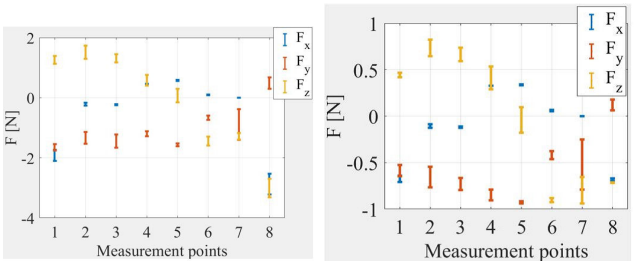

(a) (b)

FIGURE 27. Static friction force measurement results. (a) Measured value. (b) Measured value expressed as a ratio of the friction force to combined force.

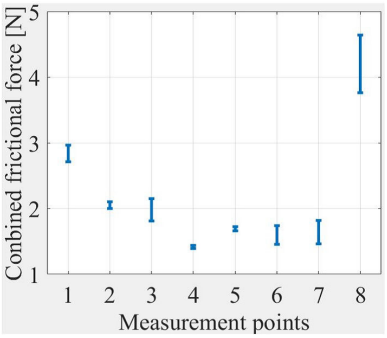

FIGURE 28. Measured results of combined static friction force.

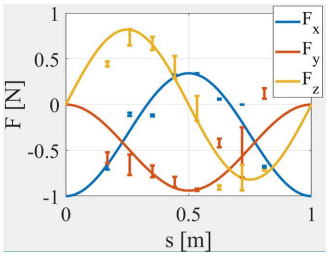

FIGURE 29. Comparison of theoretical and measured results.

coefficients of the ground and sensor surfaces are 0.191 and 0.337, respectively. The number of links of the robot was set to 16 so that the obstacle-contacting part could be sufficiently formed. In this experiment, the torsion angle between the grounding part and obstacle-contacting part was set as 0°.

B. MEASUREMENT RESULTS

1) MEASUREMENT RESULTS OF STATIC FRICTION FORCE

The results of the static friction forces F_x, F_y, and F_z in the x, y, and z directions at measurement points 1-8 are shown in Fig. 27a with error bars representing the standard deviation of the three measurements.

Fig. 27a is the result of the sensor measurement. However, the combined static friction force is not constant because the direction and amount of normal force differ at each measurement point. As shown in Fig. 28, in this experiment, the combined static friction force was different at each measurement point. The purpose of this experiment was to determine

the trend in which the directional component of the friction force is larger at the contact point. Therefore, as illustrated in Fig. 27b, the measured values are evaluated by expressing them as a ratio to the combined static friction force.

To compare the theoretical values with the measurement results, we calculated the curve length s at the obstacle-contacting part for each measurement point. To obtain the curve length s, we first determined the distance from the head of the robot to each measurement point at the initial position. This was obtained from the link number of each measurement point counted from the head of the robot (link number 5 for measurement point 1) and a link length of 70 mm. The curve length of each measurement point on the obstacle-contacting part was obtained by subtracting the length of the grounding part from this length. As with the other plots, normalization was performed by setting the beginning of the obstacle-contacting part to zero and the rear end to one. These results are plotted together with the theoretical values obtained in Section III for torsion angle $\psi = 0$ as shown in Fig. 29. This figure shows that the change in the static friction force component in each direction exhibits a similar trend between the theoretical and measured values.

First, the absolute value of F_x is large at both ends of the obstacle-contacting part (measurement points 1 and 8) and small near its midpoint (measurement points 2-7). Furthermore, the value of F_x was positive at measurement points 4 and 5. When the static friction force component in this direction is negative, it acts in a direction opposite to the direction of propulsion of the robot. Therefore, when this force is negative and its absolute value is large, as at measurement points 1 and 8, it interferes with the robot's propulsion.

Next, it can be observed that the absolute value of F_y tends to be small at both ends of the obstacle-contacting part and large near its midpoint. The static friction force in this direction causes the robot to move in the y direction in 26a. Therefore, if the absolute value of F_y is large, it is difficult to maintain contact with the obstacle.

Finally, the value of F_z is found to be positive and large at the front end of the obstacle-contacting part, and negative and large at the rear end. The negative values of F_z act vertically downward, implying that the force pushes the robot against the ground. In the experiment, the robot was pushed hard against the ground when it made contact at points 7 and 8. This increases the friction force with the ground, which often results in an overload error in the joints. At measurement points 1-3, where this value was positive and large, the robot was able to slide and propel itself owing to its weight. However, depending on the friction coefficients of the obstacle surface or the ground, the robot may climb vertically upward at these contact points by this friction force, which may interfere with the robot's propulsion.

Thus, we believe that the theory described in Section III is generally correct. However, there is a slight difference between the theory and experiment results, especially for F_y, and we discuss the cause of this difference below. First, at measurement points 1 and 2, the value of F_y should be slightly closer to 0 N, but it is approximately -0.6 N. This may be due to the slight rolling of the robot link during the shift control. This rolling pushes the sensor surface in the y-axis direction, and this force is added to the friction force owing to movement in the robot's body axis direction. Therefore, this value is considered large in the negative direction. The other measurement points do not exhibit a large amount of rolling. Measurement point 1 is the transition point from a helix to a straight line; therefore, rolling is considered to have occurred. Additionally, as shown in Fig. 29, F_y at the measurement point 8 should not be positive in this experiment from the theoretical value, but it is positive in the result. This may also be because the sensor surface is pushed due to the slight rolling that occurs during shift control, as described above. Furthermore, because the value of F_y is close to 0 N in this area of the obstacle-contacting part, the positive and negative values can be easily reversed.

2) MEASUREMENT RESULTS OF THE NORMAL FORCE

Fig. 30a shows the results of the normal force measurement with error bars indicating the standard deviation. It can be observed that the measured values are considerably larger at both ends of the obstacle-contacting part.

Then, we consider that the robot utilizes N_x, which is the normal force component in the x-direction for propulsion. The normal force component is obtained as $N_x = N \cdot \cos\gamma \cdot \cos\beta$. N_x at each measurement point is shown in Fig. 30b. This plot shows that the value of N_x is small at the midpoint of the obstacle-contacting part and increases toward both ends. In other words, a larger normal force is required for propulsion at both ends of the obstacle-contacting part. Therefore, it can be inferred that contact at these points of the obstacle-contacting part is more difficult to propel than contact at the midpoint.

One of the causes of this is the effect of friction force F_x and F_z, that interferes with propulsion. Fig. 27b shows that F_x is negative and large at both ends of the obstacle-contacting part. Additionally, the absolute value of F_z is also large at this area. Therefore, the normal force required for propulsion is expected to increase accordingly.

Another reason is related to the direction of the normal force that the robot receives from the obstacle. As shown in Fig. 23, the absolute value of the angle θ_B increases at both ends of the obstacle-contacting part such as measurement points 1 and 8. In other words, the normal force acted vertically away or towards the ground. At measurement point 8, where the sensor surface was facing downward, the normal force pushes the robot against the ground, and the friction force with the ground increases. At measurement point 1, where the sensor surface was facing upward, the robot's weight was also added to the pushing force, and the friction force with the sensor face was considered to have increased. These forces interfere with the propulsion of the robot, and the normal force required for propulsion increases.

From the above, it was deduced that the required normal force is relatively small when the robot contacts the obstacle

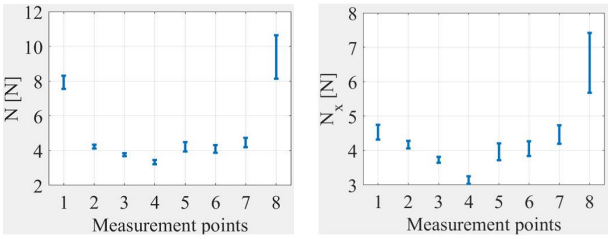

(a) Combined normal force. (b) Propulsive component of the normal force N_x.

FIGURE 30. Normal force measurement results.

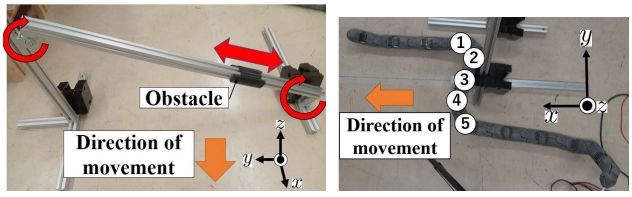

(a) Experimental apparatus. (b) Contact point number.

FIGURE 31. Experimental environment of the obstacle-aided locomotion.

near the midpoint of the obstacle-contacting part, which enables easy propulsion. However, at both ends, the required normal force increases depending on the direction of the static friction and normal force, making it difficult to propel. These results are in accordance with the theory described in Section V.

VII. EXPERIMENT OF THE OBSTACLE-AIDED LOCOMOTION

To verify the theory described in Sections III-V, we observed the obstacle-aided locomotion in several obstacle environments. The robot shown in Fig. 25 was also used in this experiment. The experimental apparatus is shown in Fig. 31. In each experiment, shift control was performed within the range where the length and number of grounding parts did not change before and after the robot's movement. The number of links of the robots varied depending on the experiment.

A. UTILIZING ONLY ONE OBSTACLE

First, we conducted an experiment in which the robot utilizes a single obstacle to propel. In this experiment, we observed the motion of the robot when it made contact at the contact points 1-5 shown in Fig. 31b. Contact point number 1 is the head side of the obstacle-contacting part. We focused on moving sideways, rotation, and ease of propulsion during propulsion.

1) SHORT ROBOT BODY LENGTH

First, a 24-link robot was used. This robot can form one obstacle-contacting part and one grounding part in front and behind the obstacle-contacting part. The obstacle was created using a 3D printer, and the material was PLA. The coefficient of static friction between the robot and obstacle was 0.141. The same experiment was conducted by increasing the coefficient of static friction to 0.264 by applying tape to the surface of the obstacle. In both experiments, we focused on the change in the position of the grounding part of the robot before and after motion, as shown in Fig. 32.

First, from Fig. 32 for the rotation, we observe that the rotation is counterclockwise at contact points 1 and 2 and clockwise at contact points 4 and 5. Let $\theta_{rot_1}, \theta_{rot_2}, \ldots \theta_{rot_5}$ be the rotation angles of the grounding part at contact points 1-5. We observe that $\theta_{rot_1} > \theta_{rot_2}$ and $\theta_{rot_5} > \theta_{rot_4}$. However, there was no significant difference in the angle of rotation between the two cases. In contrast, almost no rotation occurred at contact point 3. We compare this result with the theory of rotation described in Section IV-B. Fig. 17, when the friction coefficient μ is small, shows that the absolute value of the moment is larger near both ends of the obstacle-contacting part (contact points 1, 2, 4, and 5). In contrast, it is almost 0 N·m near the midpoint of it (contact point 3). The static friction coefficient in this experiment was relatively small at 0.141. Therefore, the results of this experiment almost corresponded with this theory. According to Fig. 17, when the coefficient of the friction is large, the moments at the contact points 1 and 5 should be small, making the robot difficult to rotate. However, similar results were obtained when the static friction coefficient was increased by applying tape to the obstacle surface. This is because, in the experiment, the difference of the static friction coefficients between two cases was small. They were 0.141 and 0.264 with and without tape respectively; thus, it is difficult to imagine that a large difference would appear. Moreover, if the friction coefficient on the surface of the obstacle is further increased, the problem described in Section V is likely to occur, and the robot cannot propel. Therefore, theoretically, the value of the moment at each contact point varied with the friction coefficient, as shown in Fig. 17. However, this could not be confirmed because, in practical terms, a large static friction coefficient would make propulsion of the robot impossible.

Sideways movement was not observed at any of the contact points when the friction coefficient was small. Even at contact point 3, which was most likely to generate sideways movements in Section IV-A, this movement was not observed. This motion is caused by the y-directional component of friction force F_y. In this case, due to small friction coeeficient, F_y was insufficient to cause the entire robot to move sideways. Additionally, the direction in which the robot moves owing to F_y should be the negative direction of the y-axis in the figure. However, as shown in Fig. 32c, the robot moves in the positive direction of the y-axis in this experiment. As shown in Fig. 16, when the effect of the friction force is small, near the midpoint of the obstacle-contacting part, the reaction force on the robot is slightly positive along the y-axis. Therefore, it is considered that the robot moved slightly in the direction of movement caused by the reaction force and not in the direction of friction force F_y. The experimental results for the case with a large friction coefficient show sideways movement at contact point 3, as shown in Fig. 33 compared to Fig. 32c. Owing

to the sideways movement, the contact point moves slightly closer to the end side of the obstacle-contacting part, which causes a slight rotation in the latter phase of the shift control. The results for the other contact points are almost the same as those for the case with a small friction coefficient. From the above, it was deduced that not only the contact point of the obstacle-contacting part, but also the coefficient of friction with the obstacle has a significant effect on the ease of moving sideways.

Next, we discuss the interference of propulsion depending on the point of contact. In all the experiments, the robot slightly climbed up on the obstacle at contact point 1 on the front end of the obstacle-contacting part. When the static friction was small, the robot could slide down the surface of the obstacle and propel itself. However, when the static friction was large, the robot was unable to propel itself because it rose up on the obstacle. In contrast, at contact point 5, the robot was pressed down by an obstacle from above, which interfered with its propulsion. When the coefficient of friction was small, the robot could barely slide on the surface of the obstacle. However, when the coefficient of friction was large, the robot could not propel. Therefore, at both ends of the obstacle-contacting part, it became clear that the robot's load and the direction of the reaction force from the obstacle acted in the vertical direction, making it difficult to propel. These results verify the theory described in Section V.

The above results show that when the robot has a short body length and can use only one obstacle, both ends of the obstacle-contacting part seem to be contact points that should be avoided. This is because the robot may rotate considerably and not be able to propel itself. In contrast, the midpoint of the obstacle-contacting part did not generate sufficient force to prevent the robot from maintaining contact with the obstacle. Therefore, there is no need to avoid contact in this area of the obstacle-contacting part.

2) LONG ROBOT BODY LENGTH

Next, an experiment was conducted to confirm the factors that prevent the rotation of the robot, as described in Section IV-B2. To confirm the effect of the moment of inertia and moment of friction of the grounding part, the number of links of the robot was increased to 40. The obstacle-aided locomotion was observed in the same way. No tape was applied to the surface of the obstacle during this experiment. The experimental results are presented in Fig. 34. It should be noted that only the results for contact points 2-4 are shown here because the robot could not be propelled at contact points 1 and 5 in this experiment. The results show that the rotation is reduced at all the contact points thanks to the moment of inertia and the moment of friction force on the grounding part stated in Section IV-B2.

Additionally, slight sideways movements were observed at all contact points during the experiment. This may be because of an increase in the normal force required for propulsion owing to the increased weight of the robot. The friction force F_y may have increased accordingly and the sideways movement occured. Additionally, the friction force components F_x and F_z, which are factors that interfere with propulsion, also increased. Consequently, the robot could not propel well at contact points 1 and 5 at both ends of the obstacle-contacting part. These results indicate that the rotation of the robot can be reduced by increasing its body length. However, when only one obstacle is used to propel, there is a disadvantage in terms of the sideways movement and propulsion interference.

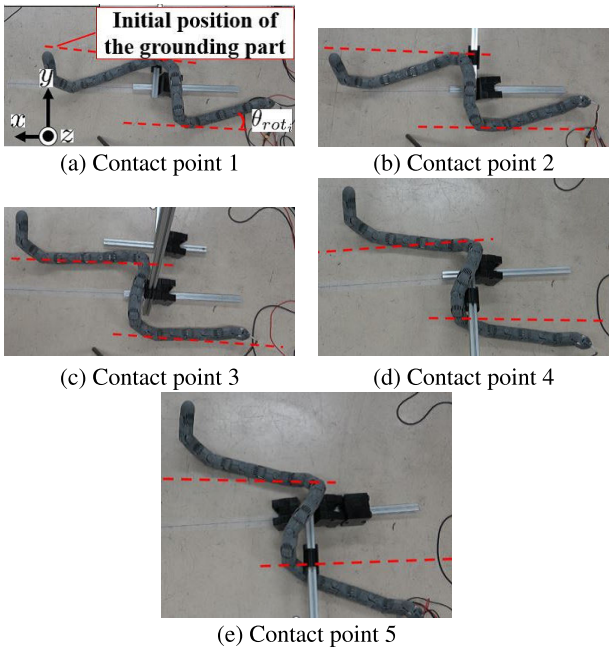

(a) Contact point 1 (b) Contact point 2

(c) Contact point 3 (d) Contact point 4

(e) Contact point 5

FIGURE 32. Experimental results when the coefficient of friction of the obstacle is small.

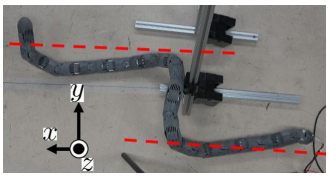

FIGURE 33. Experimental results at contact point 3 when the coefficient of friction of the obstacle is large.

B. UTILIZING MULTIPLE OBSTACLES

The same experiment was conducted using multiple obstacles. The number of links of the robot was increased to 40, and multiple experimental apparatus as shown in Fig. 31a were used.

First, we evaluated the sideways movement of the robot. As shown in Fig. 35, the experiments were conducted in which all three obstacle-contacting parts were contacted during the obstacle-aided locomotion. We compared two cases: a basic shape and a shape in which one of the obstacle-contacting parts was reversed.

Fig. 35 shows a comparison of the position of the grounding part of the robot before and after the movement. With

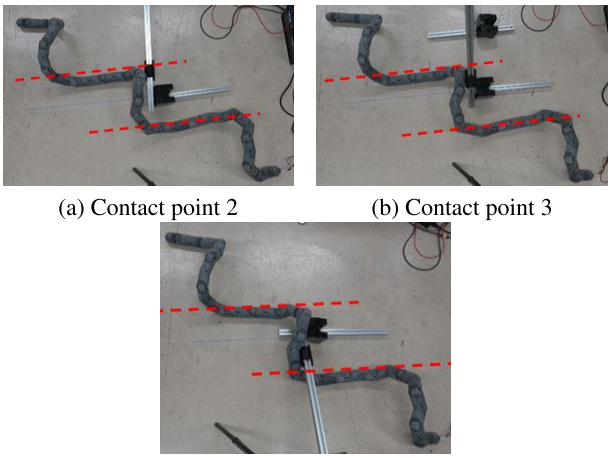

(a) Contact point 2 (b) Contact point 3

(c) Contact point 4

FIGURE 34. Experimental results when the robot's body length is long.

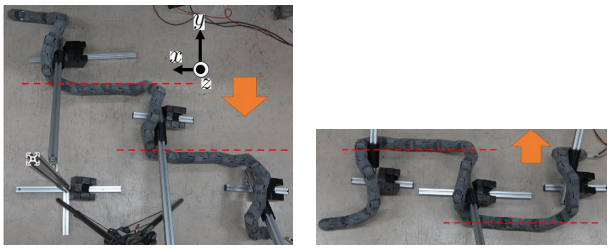

(a) (b)

FIGURE 35. Verification of the theory of moving sideways by experiments with multiple obstacles. (a) In the case of the basic shape. (b) In the case where obstacle-contacting parts are reversed.

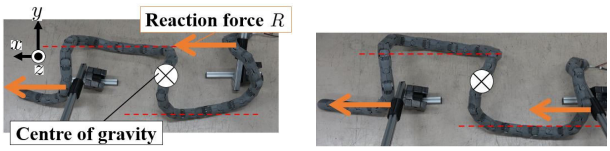

(a) (b)

FIGURE 36. Verification of the theory of rotation by experiments with multiple obstacles. (a) When moments occur in opposite directions. (b) When both moments occur in the same direction.

respect to the basic shape shown in Fig. 35a, the robot moved sideways in the $-y$ direction in the figure. However, in the case shown in Fig. 35b, the robot only moved slightly sideways in the y direction. As shown in these figures, the amount of movement is relatively smaller in the latter case. Similar results were obtained for the other contact points. In the basic shape shown in Fig. 35a, the friction force F_y of all obstacle-contacting parts is in the same direction. This is because the movement direction of the robot's body axis of all obstacle-contacting parts on the obstacle surface is the same. Therefore, it is inferred that the sum of these forces causes a relatively large sideways movement in the $-y$ direction in the figure. In contrast, in the case shown in Fig. 35b, F_y is generated in the y direction at the contact points of two reversed obstacle-contacting parts and in the $-y$ direction at one contact point of the basic one. Therefore, it is considered that the force of the difference in F_y between the two cases above causes a relatively small lateral movement in the $-y$ direction in the figure.

These results are in accordance with the theory of utilizing multiple obstacles, as described in Section IV-A. Therefore, it is necessary to adjust the number of reversed and basic obstacle-contacting parts and their contact points so that the F_y of each obstacle-contacting part cancels each other out.

Then, we evaluate the rotation of the robot. As shown in Fig. 36, the obstacle-contacting part is reversed alternately. The experiments were conducted in the case where the reaction force was obtained by two parts other than the middle of the obstacle-contacting part. We compared two contact situations, as shown in Fig. 36. Fig. 36a is a contact condition in which the moments due to the reaction forces at the two contact points are opposite each other and have almost the same value. In contrast, Fig. 36b is a contact condition in which both contact points have clockwise moments.

The results show that, in the case of Fig. 36a, the rotation of the robot was reduced as a whole. However, the grounding parts near each contact point were slightly tilted from the initial position because the robot was not completely rigid. Conversely, in the case shown in Fig. 36b, the robot rotated in the clockwise direction.

These results are in accordance with the theory described in Section IV-B. Therefore, to prevent the rotation of the robot, the contact points should be adjusted so that the moments generated at each contact point cancel each other, as shown in Fig. 36a. However, if the rigidity of the robot is low, it is inferred that the robot is slightly deformed in the direction of the moment at each contact point. Therefore, contact points with larger moments are more likely to deform, which may affect the subsequent propulsive direction.

VIII. DISCUSSION

First, we discuss the computational efficiency of this method. The CPU of the PC used in the calculations was an 11th Gen Intel(R) Core(TM) i7-1165G7 @ 2.80 GHz 2.80 GHz, and MATLAB (R2021b) was used as the programming language. In our method, the target joint angles of the robot are calculated from a continuous curve. When the body shape is changed, this continuous curve is updated and the target joint angles are recalculated. Therefore, this method is not computationally efficient. However, the average time required to define the continuous curve and calculate the target joint angles is 0.0196 s. Therefore, there is no significant impact on the robot's motion. In addition, the average computation time for calculating the reaction force and the position of the robot's center of gravity as shown in Fig. 19 is 0.161 s. Therefore, for future automation, there is no serious impact even if these analyses are performed while the robot is in motion.

In the future, based on the analysis results of this paper, we aim to develop an autonomous obstacle-aided locomotion

system. It is necessary to detect the point of contact with the obstacle for this system. This can be achieved by attaching a force sensor to the space between the motor and the exterior of each link of the robot, as in [10].

IX. CONCLUSION

In this paper, we analyze the reaction force from the obstacle during the obstacle-aided locomotion proposed in [30]. This analysis is based on the robot's target curve. Therefore, it is possible to determine if the contact state is suitable for propulsion regardless of the information on the size of the obstacle or the curvature of its surface. Additionally, the analysis can be applied to changes in the torsion angle between the grounding part and the obstacle-contacting part. Therefore, the results of this analysis can also be applied in a three-dimensional obstacle environment by connecting the obstacle-contacting part in all directions. Furthermore, compared to previous methods [8], [9], [10], [11], [12], [13], [14], [15], [16], the method proposed in this paper considers the effect of reaction forces on two-dimensional and three-dimensional planes. It is necessary to test the method in a three-dimensional obstacle scenario, such as when obstacles are above or under the robot. In the future, based on the results of this analysis, we will be able to realize autonomous three-dimensional obstacle-aided locomotion using autonomous body shape change, which will allow the robot to adapt to different environments.

REFERENCES

[1] S. Hirose and M. Mori, "Biologically inspired snake-like robots," in *Proc. IEEE Int. Conf. Robot. Biomimetics*, Aug. 2004, pp. 1–7.

[2] R. Ariizumi and F. Matsuno, "Dynamical analysis of sidewinding locomotion by a snake-like robot," in *Proc. IEEE Int. Conf. Robot. Autom.*, May 2013, pp. 5149–5154.

[3] K. Melo, "Modular snake robot velocity for side-winding gaits," in *Proc. IEEE Int. Conf. Robot. Autom. (ICRA)*, May 2015, pp. 3716–3722.

[4] M. Tanaka and K. Tanaka, "Control of a snake robot for ascending and descending steps," *IEEE Trans. Robot.*, vol. 31, no. 2, pp. 511–520, Apr. 2015.

[5] T. Takemori, M. Tanaka, and F. Matsuno, "Ladder climbing with a snake robot," in *Proc. IEEE/RSJ Int. Conf. Intell. Robots Syst. (IROS)*, Oct. 2018, pp. 8140–8145.

[6] D. Rollinson and H. Choset, "Pipe network locomotion with a snake robot," *J. Field Robot.*, vol. 33, no. 3, pp. 322–336, 2016.

[7] T. Takemori, M. Tanaka, and F. Matsuno, "Hoop-passing motion for a snake robot to realize motion transition across different environments," *IEEE Trans. Robot.*, vol. 37, no. 5, pp. 1696–1711, Oct. 2021.

[8] A. A. Transeth, R. I. Leine, C. Glocker, K. Y. Pettersen, and P. Liljebäck, "Snake robot obstacle-aided locomotion: Modeling, simulations, and experiments," *IEEE Trans. Robot.*, vol. 24, no. 1, pp. 88–104, Feb. 2008.

[9] P. Liljebäck, K. Y. Pettersen, Ø. Stavdahl, and J. T. Gravdahl, "Hybrid modelling and control of obstacle-aided snake robot locomotion," *IEEE Trans. Robot.*, vol. 26, no. 5, pp. 781–799, Oct. 2010.

[10] P. Liljebäck, K. Y. Pettersen, Ø. Stavdahl, and J. T. Gravdahl, "Experimental investigation of obstacle-aided locomotion with a snake robot," *IEEE Trans. Robot.*, vol. 27, no. 4, pp. 792–800, Aug. 2011.

[11] M. Travers, J. Whitman, P. Schiebel, D. Goldman, and H. Choset, "Shape-based compliance in locomotion," in *Proc. Robot., Sci. Syst. XII*, 2016, pp. 1–9.

[12] T. Wang, J. Whitman, M. Travers, and H. Choset, "Directional compliance in obstacle-aided navigation for snake robots," in *Proc. Amer. Control Conf. (ACC)*, Jul. 2020, pp. 2458–2463.

[13] B. Chong, T. Wang, D. Irvine, V. Kojouharov, B. Lin, H. Choset, D. I. Goldman, and G. Blekherman, "Gait design for limbless obstacle aided locomotion using geometric mechanics," 2023, *arXiv:2302.06561*.

[14] F. Ruscelli, G. Sartoretti, J. Nan, Z. Feng, M. Travers, and H. Choset, "Proprioceptive-inertial autonomous locomotion for articulated robots," in *Proc. IEEE Int. Conf. Robot. Autom. (ICRA)*, May 2018, pp. 3436–3441.

[15] T. Kamegawa, R. Kuroki, M. Travers, and H. Choset, "Proposal of EARLI for the snake robot's obstacle aided locomotion," in *Proc. IEEE Int. Symp. Saf., Secur., Rescue Robot. (SSRR)*, Nov. 2012, pp. 1–6.

[16] T. Kamegawa, R. Kuroki, and A. Gofuku, "Evaluation of snake robot's behavior using randomized EARLI in crowded obstacles," in *Proc. IEEE Int. Symp. Saf., Secur., Rescue Robot.*, Oct. 2014, pp. 1–6.

[17] T. Kano and A. Ishiguro, "Decoding decentralized control mechanism underlying adaptive and versatile locomotion of snakes," *Integrative Comparative Biol.*, vol. 60, no. 1, pp. 232–247, Jul. 2020.

[18] T. Kano, R. Yoshizawa, and A. Ishiguro, "Tegotae-based decentralised control scheme for autonomous gait transition of snake-like robots," *Bioinspiration Biomimetics*, vol. 12, no. 4, Aug. 2017, Art. no. 046009.

[19] T. Kano and A. Ishiguro, "Obstacles are beneficial to me! scaffold-based locomotion of a snake-like robot using decentralized control," in *Proc. IEEE/RSJ Int. Conf. Intell. Robots Syst.*, Nov. 2013, pp. 3273–3278.

[20] H. Date and Y. Takita, "Adaptive locomotion of a snake like robot based on curvature derivatives," in *Proc. IEEE/RSJ Int. Conf. Intell. Robots Syst.*, Oct. 2007, pp. 3554–3559.

[21] T. Sato, T. Kano, R. Kobayashi, and A. Ishiguro, "Snake-like robot driven by decentralized control scheme for scaffold-based locomotion," in *Proc. IEEE/RSJ Int. Conf. Intell. Robots Syst.*, Oct. 2012, pp. 132–138.

[22] I. Gravdahl, Ø. Stavdahl, A. Koushan, J. Løwer, and K. Y. Pettersen, "Modeling for hybrid obstacle-aided locomotion (HOAL) of snake robots," *IFAC-PapersOnLine*, vol. 55, no. 20, pp. 247–252, 2022.

[23] Y. Ozkan-Aydin, B. Liu, A. C. Ferrero, M. Seidel, F. L. Hammond, and D. I. Goldman, "Lateral bending and buckling aids biological and robotic earthworm anchoring and locomotion," *Bioinspiration Biomimetics*, vol. 17, no. 1, Jan. 2022, Art. no. 016001.

[24] Q. Fu, H. C. Astley, and C. Li, "Snakes combine vertical and lateral bending to traverse uneven terrain," *Bioinspiration Biomimetics*, vol. 17, no. 3, May 2022, Art. no. 036009.

[25] D. J. Jurestovsky, L. R. Usher, and H. C. Astley, "Generation of propulsive force via vertical undulations in snakes," *J. Exp. Biol.*, vol. 224, no. 13, Jul. 2021, Art. no. jeb239020.

[26] D. Ramesh, Q. Fu, and C. Li, "SenSnake: A snake robot with contact force sensing for studying locomotion in complex 3-D terrain," in *Proc. IEEE Int. Conf. Robot. Autom. (ICRA)*, May 2022, pp. 2068–2075.

[27] Q. Fu and C. Li, "Snake robot traversing large obstacles using vertical bending reveals importance of contact feedback for propulsion generation," 2021, *arXiv:2112.07815*.

[28] M. Vespignani, K. Melo, S. Bonardi, and A. J. Ijspeert, "Role of compliance on the locomotion of a reconfigurable modular snake robot," in *Proc. IEEE/RSJ Int. Conf. Intell. Robots Syst. (IROS)*, Sep. 2015, pp. 2238–2245.

[29] W. Zhen, C. Gong, and H. Choset, "Modeling rolling gaits of a snake robot," in *Proc. IEEE Int. Conf. Robot. Autom. (ICRA)*, May 2015, pp. 3741–3746.

[30] T. Takanashi, M. Nakajima, T. Takemori, and M. Tanaka, "Obstacle-aided locomotion of a snake robot using piecewise helixes," *IEEE Robot. Autom. Lett.*, vol. 7, no. 4, pp. 10542–10549, Oct. 2022.

[31] H. Yamada and S. Hirose, "Study of active cord mechanism-approximations to continuous curves of a multi-joint body," *J. Robot. Soc. Jpn.*, vol. 26, no. 1, pp. 110–120, 2008.

[32] T. Takemori, M. Tanaka, and F. Matsuno, "Gait design for a snake robot by connecting curve segments and experimental demonstration," *IEEE Trans. Robot.*, vol. 34, no. 5, pp. 1384–1391, Oct. 2018.

[33] D. Ding, Y.-H. Lee, and S. Wang, "Computation of 3-D form-closure grasps," *IEEE Trans. Robot. Autom.*, vol. 17, no. 4, pp. 515–522, Aug. 2001.

TAKURO TAKANASHI received the B.Eng. degree from the Department of Mechanical and Intelligent Systems Engineering, The University of Electro-Communications, Tokyo, Japan, in 2021, where he is currently pursuing the M.Eng. degree.

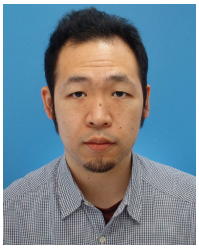

MIZUKI NAKAJIMA received the B.Eng., M.Eng., and Ph.D. degrees in engineering from the Department of Mechanical Engineering and Intelligent Systems, The University of Electro-Communications, in 2014, 2016, and 2020, respectively. He is currently a Project Assistant Professor with the Department of Mechanical Engineering and Intelligent Systems, The University of Electro-Communications. His research interest includes the development and control of snake robots.

TATSUYA TAKEMORI received the B.Eng., M.Eng., and Ph.D. degrees in engineering from the Department of Mechanical Engineering and Science, Kyoto University, in 2016, 2018, and 2021, respectively. He is currently with Abstract Engine Company Ltd., Tokyo, Japan. His research interests include biologically inspired robotics, entertainment computing, and rescue support systems in fires and disasters. He was a recipient of the Japan Society of Mechanical Engineers Award, in 2019, and the Institute of Systems Control and Information Engineers Young Researcher Award, in 2020. The collaboration for this research was primarily conducted during the author's affiliation with Kyoto University.

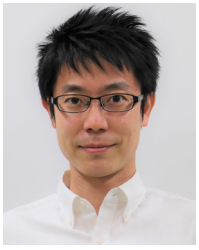

MOTOYASU TANAKA (Member, IEEE) received the B.Eng., M.Eng., and Ph.D. degrees in engineering from the Department of Mechanical Engineering and Intelligent Systems, The University of Electro-Communications, Tokyo, Japan, in 2005, 2007, and 2009, respectively. From 2009 to 2012, he was with Canon Inc., Tokyo. He is currently a Professor with the Department of Mechanical and Intelligent Systems Engineering, The University of Electro-Communications. His research interests include biologically inspired robotics and dynamic-based nonlinear control. He was a recipient of the IEEE Robotics and Automation Society Japan Chapter Young Award from the IEEE Robotics and Automation Society Japan Chapter in 2006 and the Best Poster Award at SWARM2015: The First International Symposium on Swarm Behavior and Bio-Inspired Robotics, Kyoto, Japan, in 2015.